PAPER

Check for updates

Utilization of a mixed matrix membrane modified by novel dendritic fibrous nanosilica (KCC-1-NH-CS₂) toward water purification

Mehdi Mahmoudian,* Mahsa Anvari Gharabaghlou and Nasrin Shadjou ᴵᴰ *

Various nanostructures have been used to improve the performance of nanocomposite membranes. Dendritic fibrous nanosilica (DNFS) is a new nanostructure and its performance as an adsorbent for the removal of pigments has been investigated. In this study, a type of modified dendritic fibrous nanosilica containing CS_2 groups (KCC-1-NH-CS_2) was synthesized and inserted as an additive into nanocomposite acrylonitrile–butadiene–styrene (ABS) membranes. Due to its high surface area and unique functional groups, this additive can improve the membrane's ability to remove dyes from aqueous media. Synthesized nanostructures and membranes were characterized by different analysis. The results showed that the water contact angle as a measure of surface hydrophilicity in membrane M_5 compared to membrane M_1 decreased from 79° to 67°. Water absorption (swelling degree) in membrane M_5 increased by more than 100% compared to the bare membrane. Also, this membrane, despite having high porosity (42%) and improved flux (35 L m^{-2} h^{-1}), has a better efficiency in removing dyes (MG: 99%, MB: 98%, MO: 82%) in comparison with other reported works.

1. Introduction

In recent years, the scarcity of available water resources has become a major problem for human societies and has high-lighted the importance of water as a source of life. This limi-tation has led to attention to water treatment and recovery processes.[1–4]

Despite the existence of different methods such as adsorp-tion, coagulation, distillation, boiling, and chlorination, today the use of membrane-based technologies has received more attention and this is due to the advantages of using membranes such as excellent performance, ease of processing and low operating costs.[5–10] The membrane is a semi-permeable, porous layer that removes contaminants from the water by mecha-nisms such as screening, diffusion, and interactions, and consequently purified water passes through it. Membranes used in the water treatment process, according to the material of the matrix, can be divided into two main categories: inorganic and polymeric membranes.[11–18] Inorganic membranes are often made of ceramic and have high mechanical strength; however, due to the restrictions in their manufacturing process, polymer membranes are receiving more attention and extensive research is being done to improve their performance.[19–23]

Various polymers such as polysulfone, cellulose acetate, polyvinylidene fluoride, and polyacrylonitrile have been used in

the preparation of membranes due to their high mechanical, chemical, and thermal stability, good solubility in organic solvents, and film-forming ability. However, the high cost of these polymers is a major challenge for their application in membrane fabrication. Poly(acrylonitrile–butadiene–styrene) (ABS) is a commercial terpolymer that is considered as an alternative to other polymers due to its low cost, good mechanical properties, chemical resistance and suitable pro-cessing characteristics.[23] Some studies have been done on ABS membranes. Kamelian *et al.*,[24] investigated the effect of solvent and non-solvent type on the morphology and performance properties of ABS membranes. This research group prepared and identified nanocomposite ABS membranes containing TiO_2 and Al_2O_3 nanoparticles.[25] In another study, ABS membrane was used for dewatering of *Chlorella sorokiniana* microalgae strain.[26]

As mentioned, polymeric membranes have less mechanical strength compared to ceramic membranes and also their hydrophobic nature causes problems such as fouling, reduced flux and separation efficiency.[4] With the advancement of nanotechnology, widespread studies have been conducted to use the benefits of ceramic nanomaterials in polymeric membranes to overcome their disadvantages.[27] Thus, a new class of nanocomposite membranes containing inorganic fillers has been developed, which are called Mixed Matrix Membranes (MMMs).[28] A variety of nanomaterials including carbon nano-tubes (CNT), graphene, quantum dots, different clays, metal oxides, SiO_2, and Al_2O_3 have been used in nanocomposite membranes.[29]

Nanotechnology Department, Faculty of Science and Chemistry, Urmia University, Urmia, Iran. E-mail: m.mahmoudian@urmia.ac.ir; n.shadjou@urmia.ac.ir; Tel: +98(44) 33363311

Dendritic fibrous nanosilica (DNFS) is a new type of inorganic nanostructures that was first synthesized by Polshettiwar et al.,[30] and due to its unique structure (high surface area and robust properties) it has been used quickly in many applications. The ability to functionalize of this nanostructure due to the presence of large amounts of (Si–OH) groups is the main advantages and can significantly improve its performance. Modified DNFS has previously been used by our research group as an adsorbent to remove malachite green (MG) and also as an additive in polyphenylsulfone nanocomposite membranes.

In this study, thiocarbamate functional groups were attached to the pores and channels of Novel fibrous shaped silica nanospheres, denoted as KCC-1 (KAUST Catalysis Center) through the linking group on the surface of DNFS and then this compound was used as an additive in ABS nanocomposite membranes. The formation of thiocarbamate groups due to its ability as ligand can have a significant effect on the removal of water-soluble contaminants. For this purpose, the efficiency of membranes in removing Malachite green (MG), Methylene blue (MB), and methyl orange (MO) dyes has been evaluated.

2. Experimental

2.1. Materials

Acrylonitrile–butadiene–styrene (ABS) was provided from Samsung (South Korea, tradename ABS Starex SD-0150). Polyethylene glycol (PEG) (M_w: 10 000 g mol^{-1}), N-methyl pyrrolidone (NMP), dimethyl sulfoxide (DMSO), triethyl amine, carbon disulfide, tetraethyl orthosilicate (TEOS), and cetyltrimethylammonium bromide (CTAB) were purchased from Merck. Dioctyl adipate (DOA), 3 amino propyl triethoxy silane (APTES), and methylene blue and methyl orange were supplied from Sigma-Aldrich. All the mentioned materials were used as received without further purifications.

2.2. Synthesis of KCC-1, KCC-1-NH$_2$, and KCC-1-NH-CS$_2$

The synthesis of KCC-1 and modified species was performed according to the method presented in ref. 31. For the synthesis of KCC-1, briefly, 1 g CTAB was added to 10 mL deionized water and after addition of 0.6 g urea, the mixture was stirred for about 3 h at room temperature. Then, the mixture of 2 g TEOS, 30 mL cyclohexane and 1.5 mL hexanol was added to the flask and sonicated for 30 min. Afterwards, the mixture was refluxed at 120 °C for 4 h and subsequently refluxed at 80 °C for 24 h. Next, the mixture was cooled to the room temperature and centrifuged to collect the KCC-1 as white sediment. The collected KCC-1 was washed several times with water and ethanol and dried at 60 °C for 24 h. Finally, the as-synthesized KCC-1 was calcinated at 550 °C for 6 h to remove the CTAB as templating agent. As mechanism of the KCC-1 synthesis, urea was used to hydrolyze the TEOS to produce negatively charged $(SiO_4)^{4-}$ silicate. Using of CTAB induces the silicate molecules to form self-assembled linear structures where the CTAB helps to the aggregating of the silicates.[30]

For the functionalization of KCC-1-NH$_2$ by dithiocarbamate, 20 ml of acetonitrile comprising 1% Et$_3$N. The obtained solution was stirred overnight. Finally, the mixture was dried by evaporator. KCC-1-NH-CS$_2$ was added to copper(II) sulphate solution (1 M, 25 ml in deionized water) and stirred at 60 °C for 15 h. The obtained nanocatalyst was separated with a centrifuge and washed successively with water (3 × 10 ml) and finally dried in vacuum at room temperature to give the Cu@KCC-1-NH-CS$_2$ and 90 mg of KCC-1-NH$_2$ was mixed with 100 mg of CS$_2$.

2.3. Fabrication of membrane

Nanocomposite membranes were prepared by phase inversion procedure. In this method, the ABS solution was prepared as 20% wt in the NMP and then PEG (10% wt) and DOA (20% wt) were added to the solution. In the preparation of various formulations, KCC-1-NH-CS$_2$ was incorporated into the solution as additive with weight percentages of 1 to 7 and completely dispersed under ultrasonic stirring. The resulting mixtures were spread on the glass surface with a thickness of 200 μm (by a film applicator) and immediately immersed in a deionized water bath as a non-solvent. After separating from the glass surface, the membranes were kept in water for 24 hours and then dried in vacuum oven at 50 °C. The composition of the fabricated membranes is given in the Table 1.

2.4. Instruments

The Fourier-transform infrared spectroscopy (FTIR) technique was used to investigate the chemical structure of nanostructures and prepared membranes. The scanned range was between 400 and 4000 cm^{-1} (WQF-510A spectrophotometer). The Field emission scanning electron microscopy (FESEM, HITACHI S-4160) and transmission electron microscopy (TEM, Philips CM 100 Biotwin Electron Microscope operated at 75 kV) analyzes were used to investigate the shape and size of the particles as well as the morphology of the membranes. To examine the surface roughness, images were prepared using an atomic force microscopy (AFM, DME-SPM Semilab). Energy dispersive X-ray (EDAX) and image mapping techniques were used to demonstrate the modification performed on KCC-1 and the dispersion of particles in the membrane matrix. The mechanical strength of the membranes was studied using a tensile test. The experiment was performed according to the ASTM D412 standard method and using a FRANK-PTI Horizontal Tensile Tester. Zeta potential test was used to measure the surface charge of membranes (HORIBA Scientific, SZ-100).

Table 1 The composition of nanocomposite membranes

Membrane	ABS (% wt)	KCC-1-NH-CS$_2$ (% wt)	PEG (% wt)	DOA (% wt)
M$_1$	20	0	10	20
M$_2$		3		
M$_3$		5		
M$_4$		7		
M$_5$		10		
M$_V$^{a}		5		

^{a} In membrane M$_V$, the incorporated additive is KCC-1.

2.5. Water uptake measurement

To perform this test, a piece of membrane with a surface area of 1 cm^2 was cut and completely dried for 24 hours at 50 °C in a vacuum oven. The sample was carefully weighed (W_d) and immersed in deionized water. After 24 hours, the membrane sample was removed from the water and weighed again after taking surface water (W_w). Membrane water uptake percentage was calculated using eqn (1).

$$\text{Water uptake}(\%) = \frac{W_w - W_d}{W_w} \times 100 \tag{1}$$

The measurements were repeated three times and the mean was reported as the amount of water uptake.

2.6. Measurement of porosity and pore radius in membranes

Membrane porosity was measured by gravimetric method according to the amount of swelling in deionized water (eqn (2)).

$$\varepsilon(\%) = \frac{(W_w - W_d)}{A \times l \times d_w} \times 100 \tag{2}$$

In this equation, the percentage of porosity is shown by ε. W_d and W_w correspond to the weight of dry and wet membranes in terms of grams, respectively. The d_w indicates the density of water (1 g cm^{-3}), A is the surface area of the membrane (cm^2), and l represents the thickness of the membrane (cm).

In addition, the mean pore radius of the membranes was obtained according to velocity filtration method using the Guerout–Elford–Ferry theory (eqn (3)).

$$R_m = \sqrt{\frac{(2.9 - 1.75\varepsilon) \times 8\eta l Q}{\varepsilon \times A \times \Delta P}} \tag{3}$$

R_m, η, l, Q, A, and ΔP show the mean radius of the pores (m), water viscosity (pa s), membrane thickness (m), membrane flow rate (m^3 s^{-1}), surface area (m^2), and applied pressure (pa), respectively.

2.7. Contact angle measurement

In this test, small droplets of deionized water were placed in different parts of the membrane surface and the image of the droplets was taken. The contact angle of water droplets with the surface was measured using *Image J software*. The water contact angle in different parts of the membrane surface was measured and the average was reported. Standard deviation was also calculated for the data.

2.8. Membrane performance evaluation

2.8.1. Pure water flux (PWF). A home-made nano-filtration cell was used to determine the pure water flux. The applied membrane for this test had a surface area of 3.73 cm^2 and was prepared in a circular shape. This sample was located at the membrane loading site; the tank of the cell unit was completely sealed and filled with deionized water as feed. Nitrogen gas was used as the driving force with pressures of 3 to 10 bar. The PWF was calculated using the eqn (4).

$$\text{PWF} = \frac{Q}{At} \tag{4}$$

In this regard, the PWF is measured in terms of kg m^{-2} h^{-1}. Also, Q is the amount of collected water (kg), A is the area of the membrane surface (m^2). The measurement time is indicated by t (h).

2.8.2. Dye rejection. To evaluate the effectiveness of KCC-1-NH-CS$_2$-containing membranes in removing dyes, the method similar to the above instruction was used, however as a feed, a solution of methylene blue (Mb) and methyl orange (MO) dyes with concentrations of 50 and 100 ppm was used. The permeate solution through the membrane was collected and used to calculate the dye rejection percentage (eqn (5)). The applied pressure in this test was 5 bar. A UV spectrophotometer (PG, China) with 1 cm quartz cell was used to measure the concentration of dyes.

$$\text{Rejection}(\%) = 1 - \left(\frac{C_p}{C_f}\right) \times 100 \tag{5}$$

C_p and C_f represent the concentrations of dyes in feed and permeate solutions, respectively.

Studies of membrane fouling as well as their efficiency in long-term use were performed using dye solution and flux measurement.

3. Results and discussion

In this study, the synthesized KCC-1 was modified in two steps and thiocarbamate functional groups were created on the surface of nanostructures (KCC-1-NH-CS$_2$). These modified nanostructures were introduced as additives into the membrane matrix. An overview of this study is shown in Fig. 1.

To confirm the successful modification process, the prepared nanostructures are characterized by FTIR, FESEM, TEM, BET, and EDAX.

The FTIR spectra of KCC-1 and KCC-1-NH-CS$_2$ are shown in Fig. 2. The characteristic peaks of the KCC-1 appear at 802 and 1100 cm^{-1} correspond to the symmetric and asymmetric stretching vibrations of the Si–O–Si bond, respectively. New peaks have been observed in the KCC-1-NH-CS$_2$ spectrum at 1626 cm^{-1} (deformation NH$_2$), 2520 cm^{-1} (stretching vibration of S–H in mercaptan groups), 2890 cm^{-1} (stretching vibration of aliphatic C–H), and 3400 cm^{-1} (vibration of N–H bond), which confirm the presence of the related functional groups and proves the successful modification of the KCC-1 surface.

To investigate the size, and morphology of KCC-1 and KCC-1-NH-CS$_2$, the FESEM and TEM images were recorded and shown in Fig. 3. As can be seen in FESEM images, on the surface of the KCC-1, wrinkle-like roughness can be seen, which has given them a dendritic structure. However, in KCC-
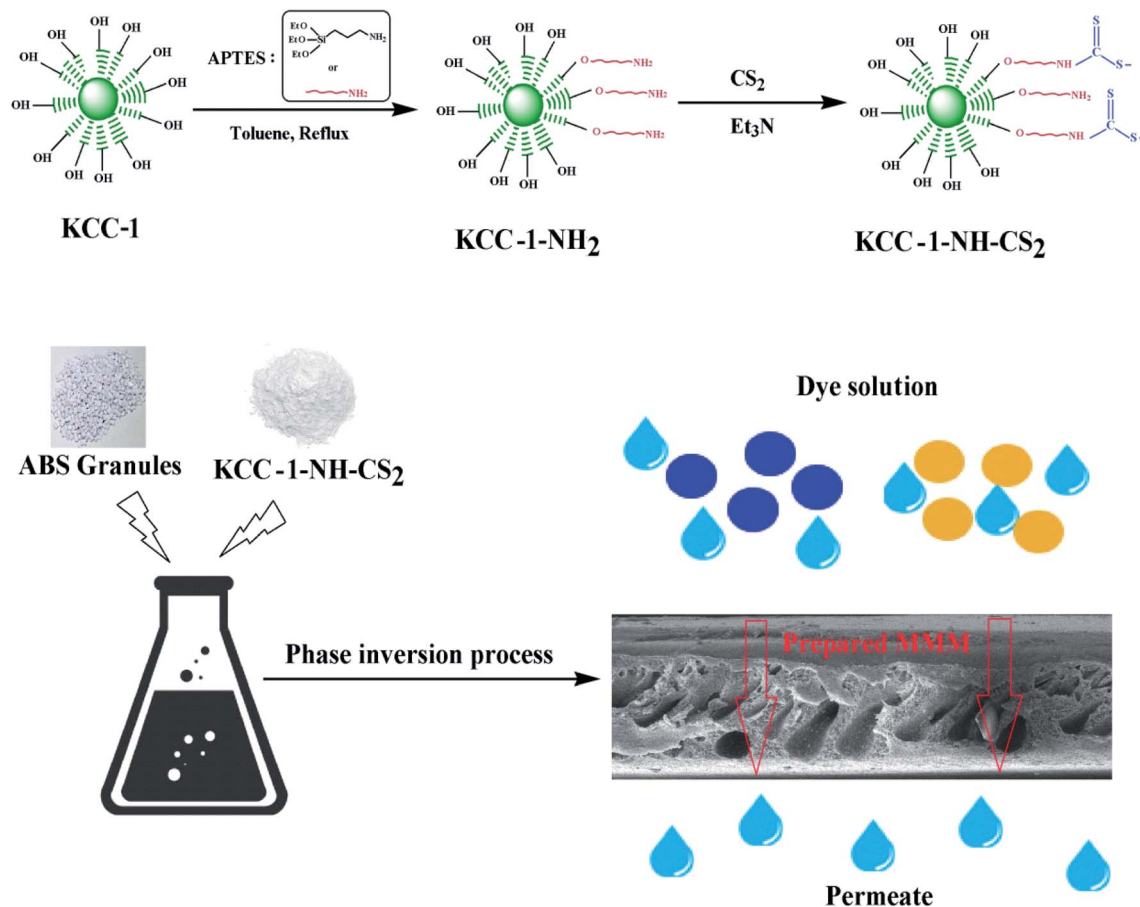
Fig. 1 The modification and fabrication steps.

1-NH-CS$_2$, the gaps between dendritic structures appear to be filled, and this filling can be attributed to the functionalization of the nanostructures.

The dendritic structure of KCC-1 is clearly detectable in the TEM image. This structure is also seen in the KCC-1-NH-CS$_2$, however there are dark spots with a distinctive color in the KCC-
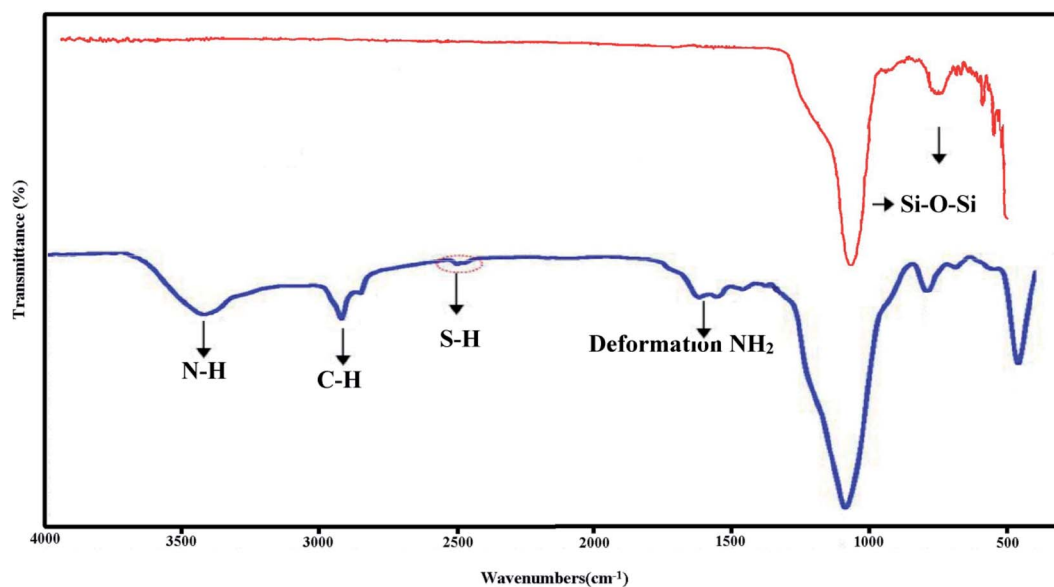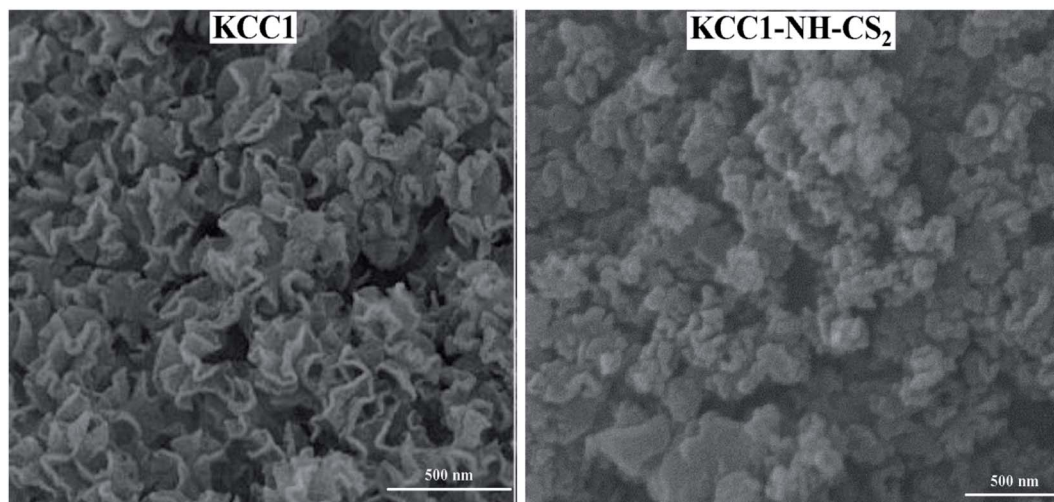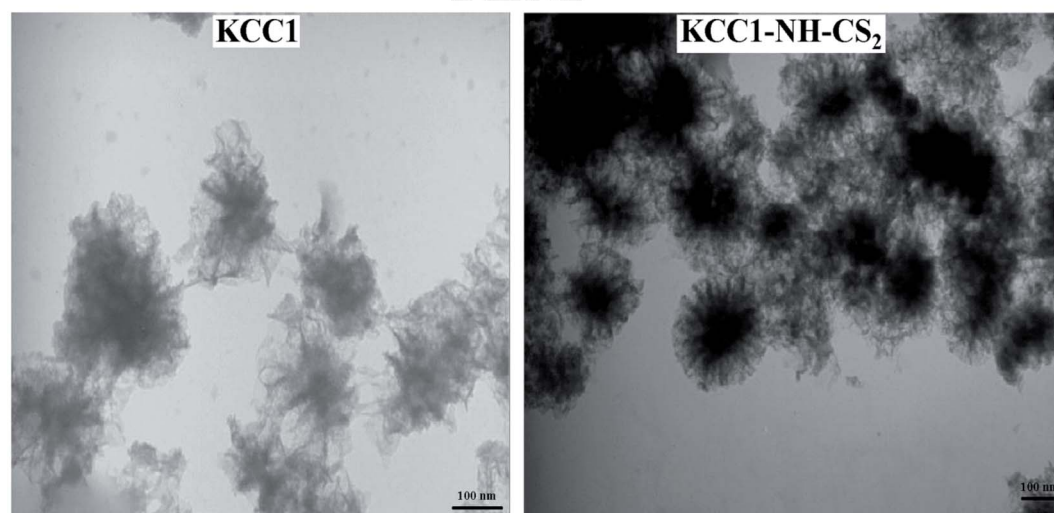

Fig. 2 FTIR spectra of KCC-1 and KCC-1-NH-CS$_2$.

FESEM

TEM

Fig. 3 FESEM and TEM images of KCC-1 and KCC-1-NH-CS$_2$.

1-NH-CS$_2$ image that may belong to new functional groups attached to the surface.

To confirm the presence of elements in the functional groups attached to the surface of the KCC-1, the EDAX (energy-dispersive X-ray spectroscopy) elemental analysis was performed on the KCC-1, KCC-1-NH$_2$, and KCC-1-NH-CS$_2$ and the results along with the composition of the elements are shown in Fig. 4. The detected elements at the KCC-1 surface included O and Si. Minor amounts of C and N have also been detected at the KCC-1 surface, which seems to be related to the impurities remaining from the KCC-1 synthesis steps. The presence of N and C is identified as the attached APTES on the surface of KCC-1-NH$_2$, and finally the observed sulfur in the KCC-1-NH-CS$_2$ can be attributed to the CS$_2$ groups linked *via* amine functionalities.

Adsorption–desorption isotherms of N$_2$ were measured at 77 K by an N$_2$ adsorption system after each sample was evacuated

at 373 K for 3 h. The surface areas and the pore size distributions were calculated by the BET and BJH method, respectively.

Porosity analysis was performed from the prepared nanostructures and the results are collected in Table 2. The findings show that by performing functionalization reactions, the surface area decreases from 617 cm^2 g^{-1} for KCC-1 to 133 cm^2 g^{-1} for KCC-1-NH-CS$_2$, the volume of pores decreases and the average pore size increases slightly. The reduction in surface area and pore volume can be due to the filling of pores and cavities in the dendritic structure of KCC-1 by the attached groups, and the observed changes confirm the functionalization reaction.

After successful functionalization of KCC-1, these modified nanostructures (KCC-1-NH-CS$_2$) are incorporated into the ABS membrane matrix as additives in different percentages and the fabricated nanocomposite membranes were identified and studied.
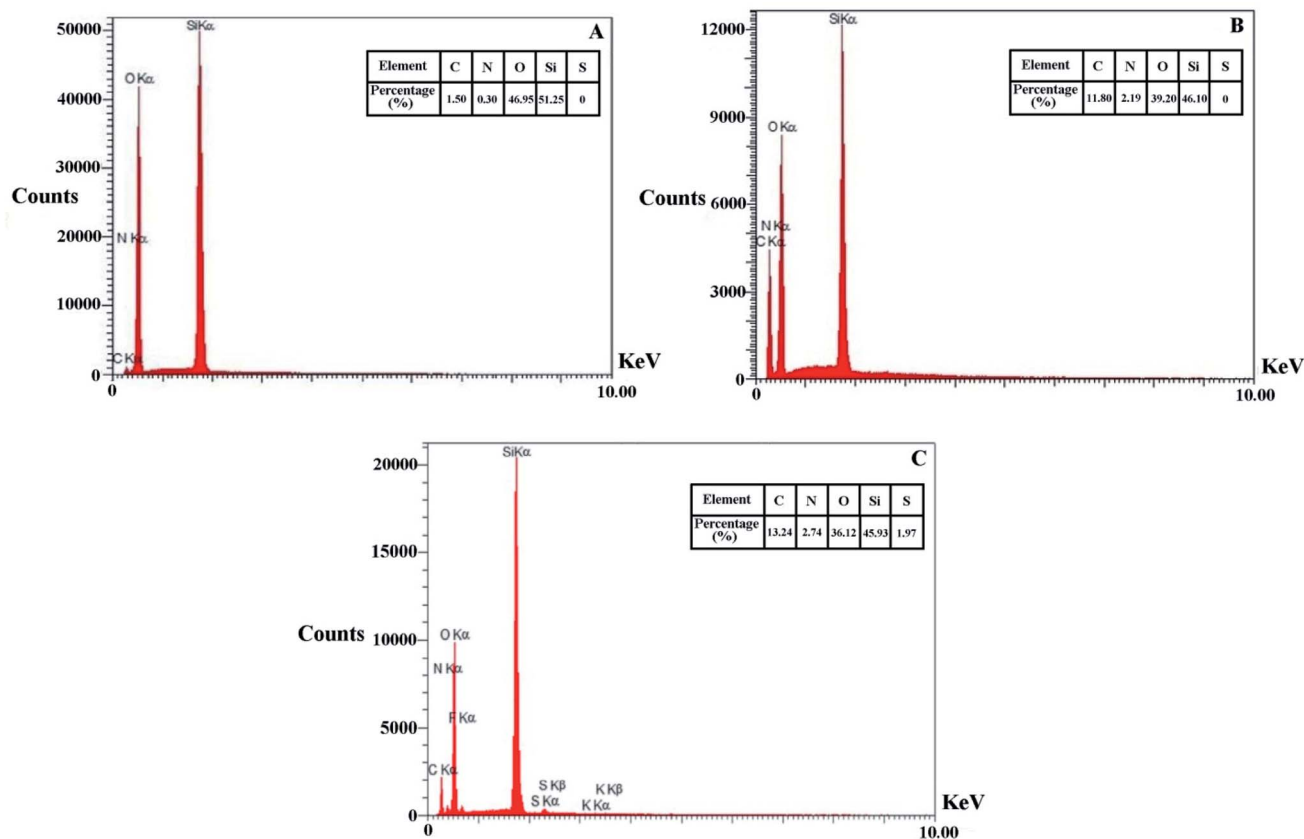
Fig. 4 EDAX elemental analysis of KCC-1, KCC-1-NH$_2$, and KCC-1-NH-CS$_2$.

Table 2 Surface area, average pore size, and volume of pore foe KCC-1, KCC-1-NH$_2$, and KCC-1-NH-CS$_2$

Sample	Surface area (m^2 g^{-1})	Average pore size (nm)	Volume of pores (cm^3 g^{-1})
KCC-1	617	9	1.5
KCC-1-NH$_2$	376	11	1.1
KCC-1-NH-CS$_2$	133	12	0.4

The morphology of the membranes is examined by providing cross-sectional FESEM images. The resulting images are shown in Fig. 5. In cross-sectional images of the membranes, an asymmetric structure consisting of a top thin dense layer on the porous layer is noticeable. With increasing percentage of additive, the porosity has increased compared to pure membrane. This porosity is clearly observable in the larger magnification of membrane M$_5$ (containing 10 wt% KCC-1-NH-CS$_2$), whereas the microstructure of membrane M$_v$ is similar to pure membrane and membranes with a low percentage of KCC-1-NH-CS$_2$.

To study the surface morphology of the membranes AFM analysis is applied. The images and results are shown in Fig. 6 and Table 3. Images and R_a and R_q results for membranes show that the pure membrane had the lowest surface roughness and with increasing additive content the roughness enhances. This increase is attributed to the improvement of membrane surface

hydrophilicity due to the migration of additives with polar functional groups, and previous studies confirm these findings.

The presence of nanostructures at the membrane surface was investigated by identifying functional groups and elements using FTIR and EDAX techniques, respectively.

The spectra of pure and nanocomposite membranes containing KCC-1 and KCC-1-NH-CS$_2$ are shown in Fig. 7. In the spectrum of neat ABS membrane, prominent peaks are seen in 730, 1480, 1650, 2237, 2920 and 3100 cm^{-1}, which are related to the CH=CH out of plane, benzene ring in aromatic compounds, C=C, C≡C, aliphatic C–H, and aromatic C–H vibrations, respectively. The spectrum of the other membranes is similar to the neat membrane, except that in membrane M$_5$, which has the highest KCC-1-NH-CS$_2$ content (10 wt%), the sharp peak appears at 1150 cm^{-1}, which is the characteristic peak of the modified KCC-1 and indicates its entry into the membrane structure. The decrease in the intensity of this peak in membrane M$_v$ may be due to the hydrophobic nature of the KCC-1 nanostructures and their non-migration to the membrane surface, while the KCC-1-NH-CS$_2$ due to the hydrophilic nature of the attached groups migrated to the surface during membrane formation and is better detected.

The results of performed EDAX elemental analysis from the surface of the membranes are shown in Fig. 8. It is observed that in membrane M$_1$, there are no elements of S and Si, while in membranes M$_3$ and M$_5$, these elements are detectable on the
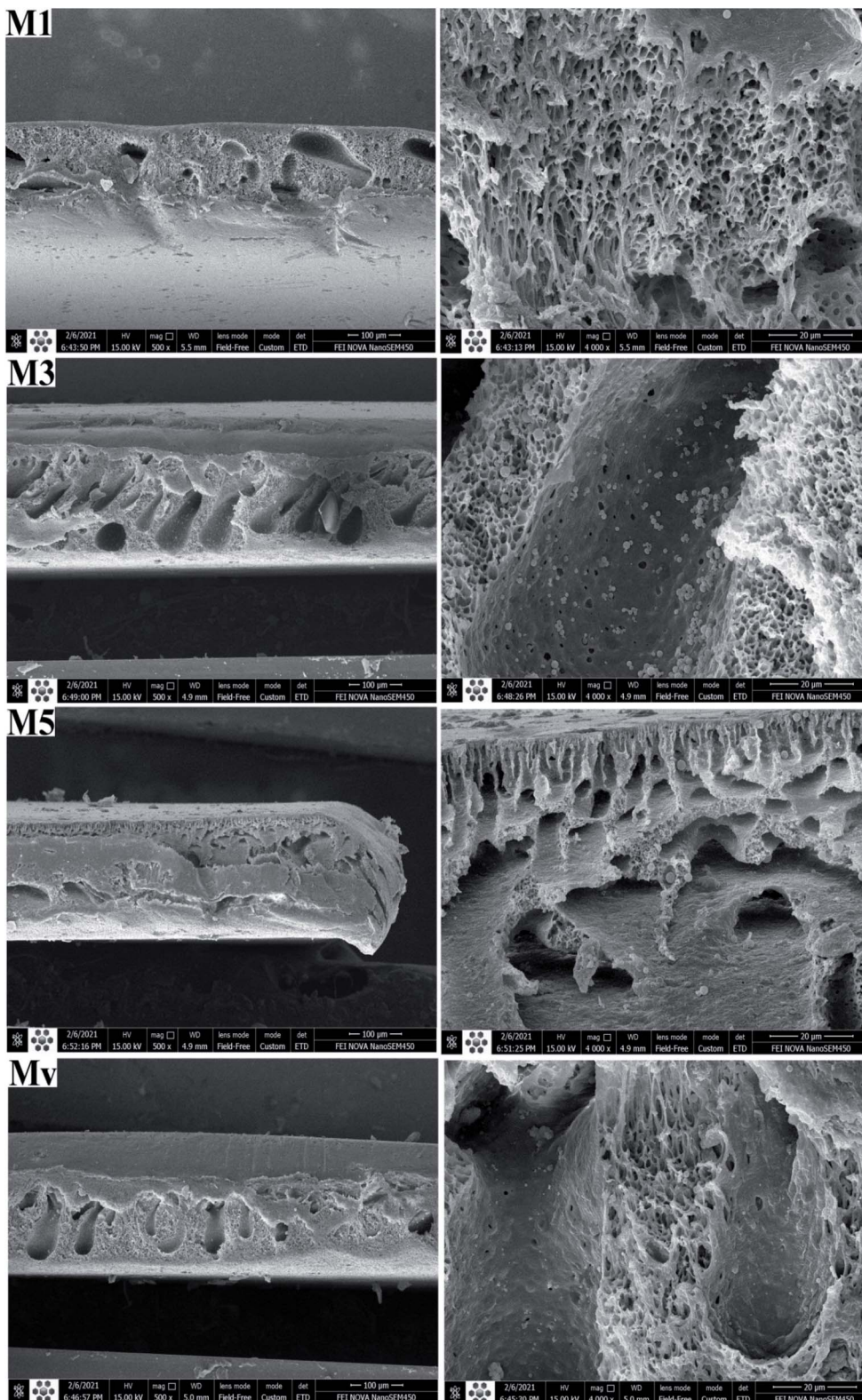
Fig. 5 Cross-section FESEM images of pure and nanocomposite membranes.

surface of the membranes. The low percentage of Si may be due to the coating of the KCC-1-NH-CS$_2$ nanostructures with the membrane polymeric matrix. S was not detected in M$_V$.

To investigate the effect of the presence of additives (KCC-1 and KCC-1-NH-CS$_2$) and their functional groups on the surface hydrophilicity, the contact angle of water with the surface of the
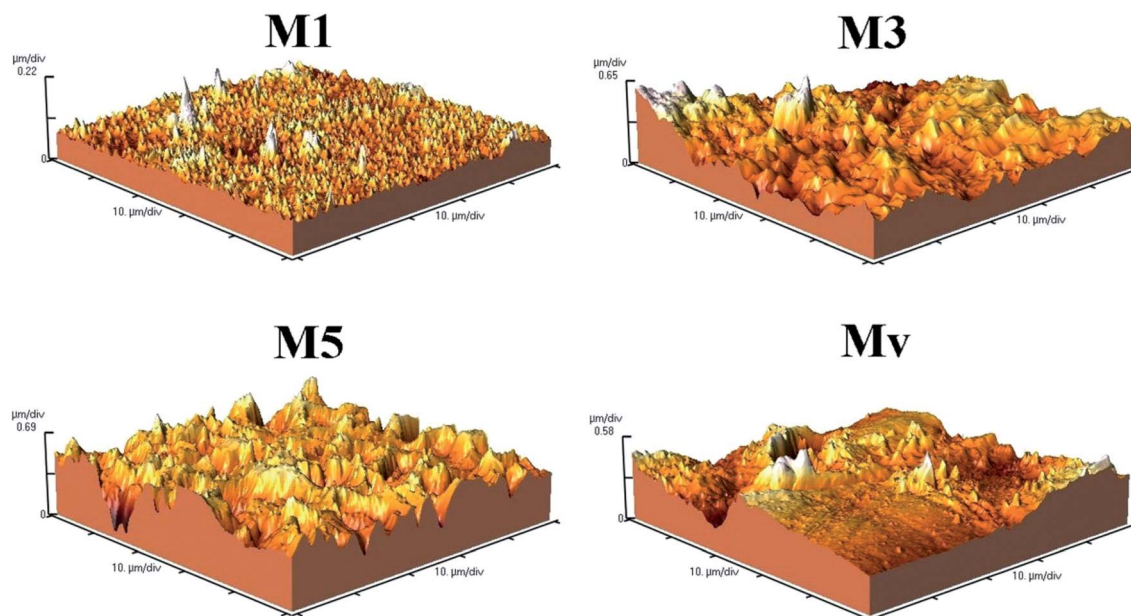
Fig. 6   AFM image of neat and nanocomposite membranes.

Table 3 R_a, R_q, and mean Ht for the prepared membranes

Entry	R_a (nm)	R_q (nm)	Mean Ht (nm)
M_1	15.75	22.41	162.20
M_3	115.60	150.51	555.60
M_5	148.10	184.60	875.30
M_v	86.70	112.60	643.90

membranes was measured and the results are shown in Fig. 9. As the surface hydrophilicity increases, the interaction of the droplet water molecules with the membrane surface increases and as a result its contact angle with the membrane surface decreases. The contact angle of water with the surface of neat membrane is 79° and gradually decreases with increasing KCC-1-NH-CS$_2$ content in nanocomposite membranes and reaches 58° in M_5 membrane. This increase in hydrophilicity can affect membrane performance (include water flux and dye rejection) and improve its efficiency. The obtained water contact angle for membrane M_v is 67° and shows less hydrophilicity than membrane M_5.

The presence of nanostructures introduced into the membrane matrix, in addition to surface hydrophilicity, can also affect the hydrophilicity of the matrix. The swelling of membranes includes absorbed water by the immersed membrane over a period of time and depends on factors such as matrix hydrophilicity and porosity. Considering that the porosity of membranes is affected by their hydrophilicity and the solvent and anti-solvent exchange rate in the coagulation bath, it can be said that the basic parameter in the rate of swelling is the hydrophilicity of the membrane matrix. The measured swelling for the neat and nanocomposite membranes is indicated in Fig. 10. It is observed that the lowest recorded swelling belongs to the neat membrane, which can be justified by the hydrophobic

nature of ABS and membrane matrix. Swelling in nanocomposite membranes is higher due to improved hydrophilicity and higher porosity. The swelling obtained for membrane M_v is lower than
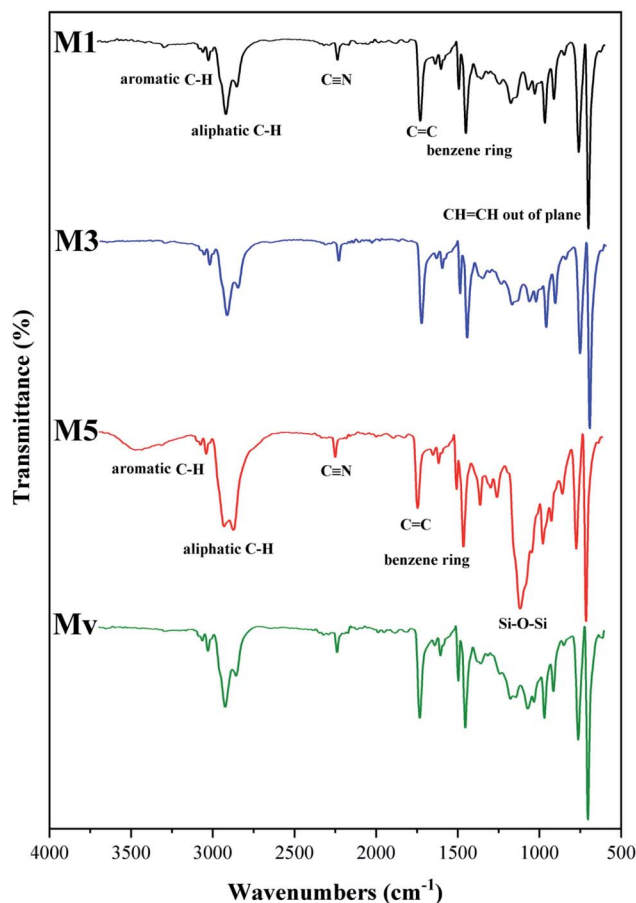

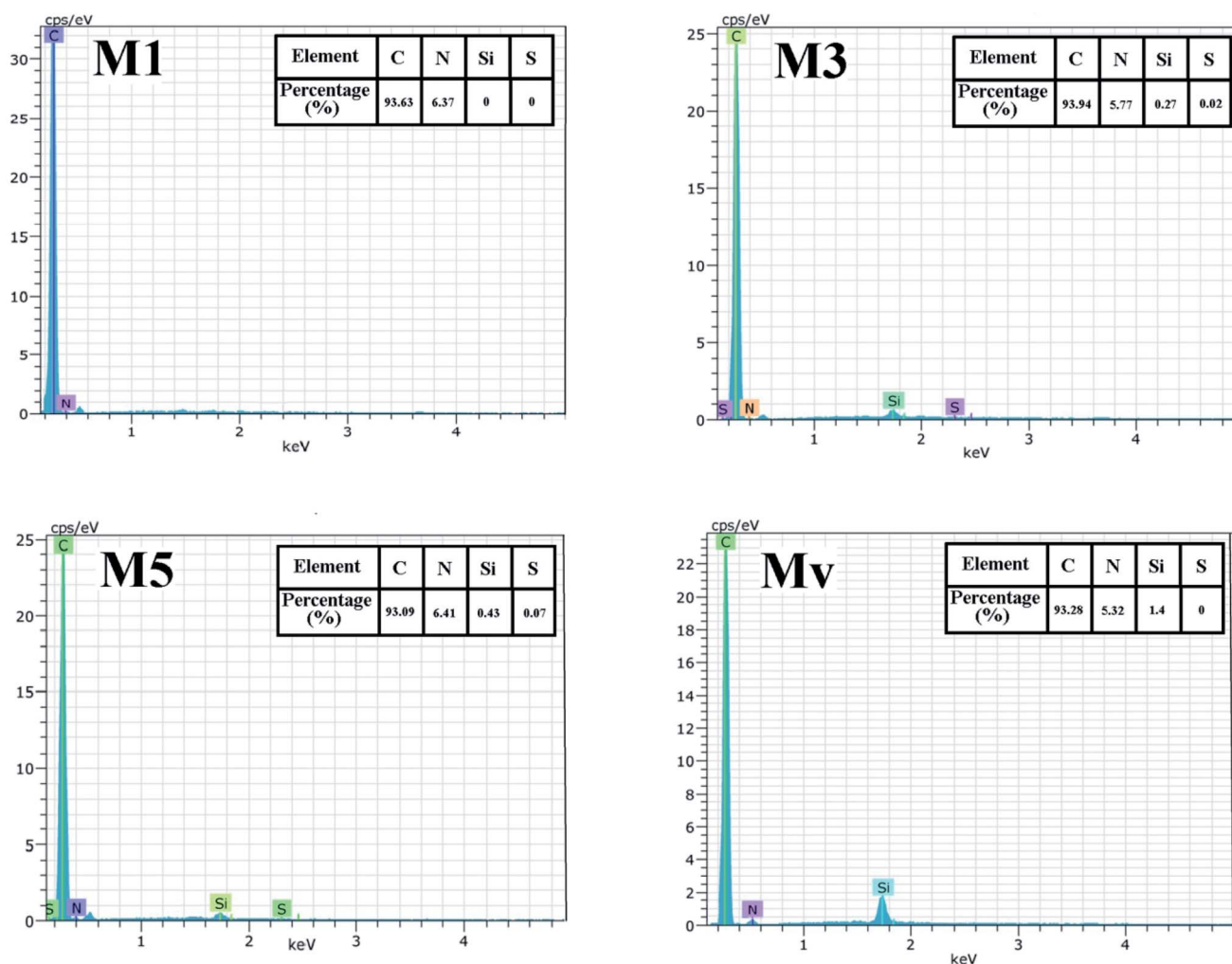Fig. 7   ATR-FTIR spectra of neat and nanocomposite membranes.

Fig. 8 EDAX elemental analysis of the prepared membranes.

nanocomposite membranes with KCC-1-NH-CS$_2$, proving the lower effect of unmodified KCC-1 on hydrophilicity (similar to water contact angle results).

To study the effect of improving the membranes hydrophilicity on porosity, porosity measurements were carried out theoretically using swelling amounts and the percentage of porosity and
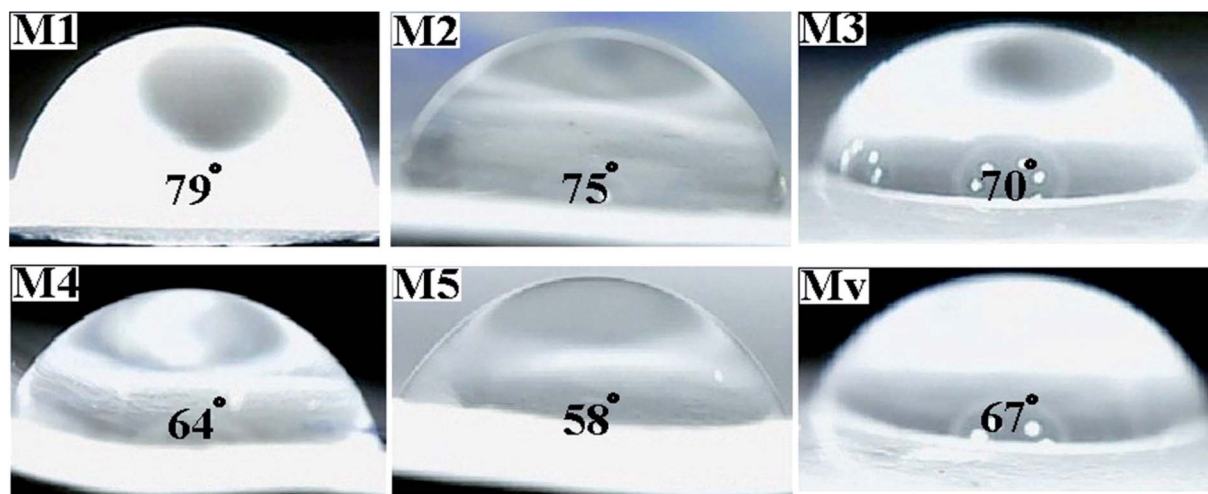

Fig. 9 Measured water contact angle for the neat and nanocomposite membranes.
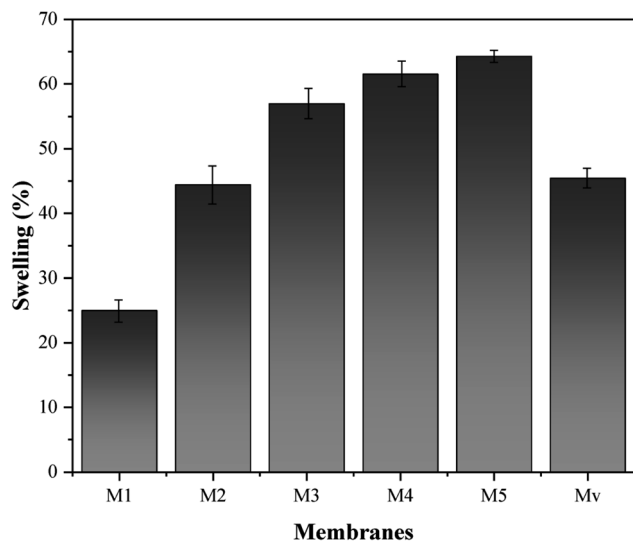
© 2022 The Author(s). Published by the Royal Society of Chemistry

Fig. 10 Measured swelling for neat and nanocomposite membranes.

Fig. 11 The pure water flux of membranes. The pressure was changed from 2.5 to 7.5 bar.

Table 4 Porosity, mean pore radius, and Zeta potentials of the prepared membranes

Entry	Porosity (%)	Mean pore radius (nm)	Zeta potential (mV)
M_1	5.9	1.1	−4.6
M_2	20	1.5	−11
M_3	38	1.84	−13.2
M_4	40	2	−19
M_5	42	2.06	−21.2
M_v	27	1.33	−14

average radius of pores were tabulated in Table 4. As expected, the porosity increased with increasing KCC-1-NH-CS$_2$ in nanocomposite membranes, from 5.9% in membrane M_1 to 42% in membrane M_5. Less porosity was also demonstrated in membrane M_v. Despite the remarkable changes in the porosity of nanocomposite membranes, the size of the pores in the membrane microstructure has not changed significantly and has increased from 1.1 nm in membrane M_1 to 2.06 nm in membrane M_5. Approximately constant size of pores can be an important advantage for nanocomposite membranes, as it does not significantly affect the performance of membranes by screening mechanism.

To survey the effect of membrane surface charge on its performance in the removal of charged dyes (MG and MB: positive, MO: negative), the zeta potential of the membrane surface is measured (Table 4). Membrane M_1 has a partial negative charge of −4.6 mV and with the incorporation of KCC-1-NH-CS$_2$, the negative charge of the surface has increased, which can be explained by the negative charge on the surface of the KCC-1-NH-CS$_2$. These charge changes can affect the performance of the membrane in rejection of charged dyes.

3.1. Performance investigation of membrane

3.1.1. Pure water flux. Pure water flux is one of the properties that is studied to evaluate the performance of the
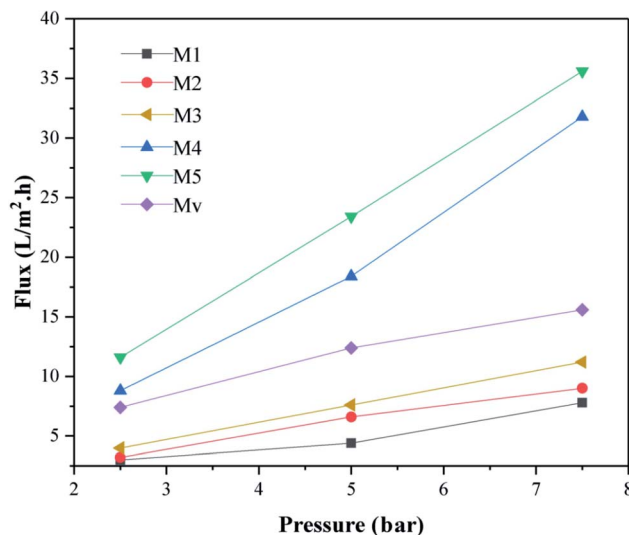
membrane and depends on parameters such as porosity, pore size and hydrophilicity of the membrane. In this study, pure water flux was measured at different pressures and the results are summarized in Fig. 11. It is observed that with increasing pressure as the driving force, the pure water flux has increased. The slope of flux with increasing pressure is higher in nanocomposite membranes, which may be due to the larger pore size of these membranes.

Moreover, the increase in pure water flux in nanocomposite membranes is quite significant with increasing the content of KCC-1-NH-CS$_2$ nanostructures, and this can be due to higher porosity and improved hydrophilicity in these membranes. The M_v Membrane shows lower water flux than membrane with the same percentage of modified KCC-1 (M_5).

3.1.2. The effect of prolonged exposure to high pressure on pure water flux. To investigate the effect of time on membrane performance, pure water flux was measured at 5 bar pressure over a 5 hour period. The findings (Fig. 12) show that pure water flux decreases in all membranes with the similar slope. This decrease in flux is due to the compaction of the membranes due to prolonged exposure to high pressure and is related to the compaction strength of the membrane. Slope stability over time indicates that the compaction strength of the membranes is not affected by the additive, while other studies have shown that the compaction strength of nanocomposite membranes decreases with increasing hydrophilic additive content. This unique feature can be due to the good compatibility of the additives with the membrane matrix.

3.1.3. Dye solution flux. To study the effect of soluble dyes in water flux through membranes, malachite green (MG), methylene blue (MB), and methyl orange (MO) dyes are selected and their solutions (5 and 50 ppm) are prepared. Then, the flux of dye solutions is measured at 5 bar pressure and obtained results are represented in Fig. 13. Similar to the observed trend for pure water flux, the highest dye flux belongs to membrane M_5 and the improvement in the performance of nanocomposite membranes
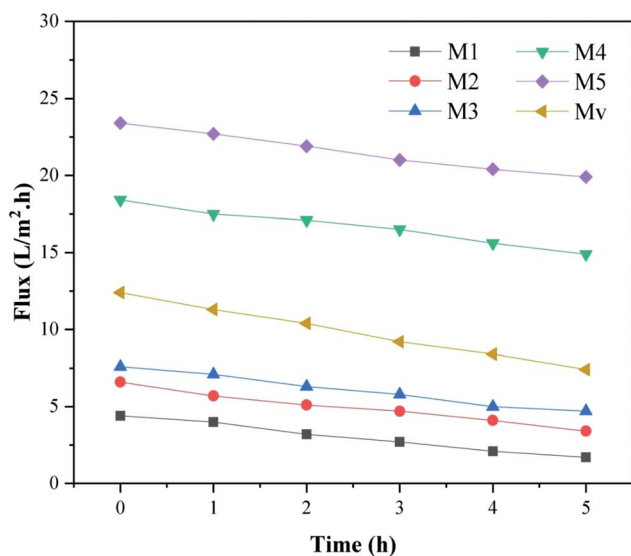
Fig. 12 Decreased water flux observed in membranes over time (0–5 h).

in passing water compared to the pure membrane is significant. Dye flux of membrane M_v has decreased compared to membranes with a high percentage of KCC-1-NH-CS$_2$.

Interestingly, dye flux is reduced at high concentrations (50 ppm), which may be due to the blockage of part of the membrane pores by the dyes. On the other hand, MG has the lowest flux and MO has the highest flux. MB (positive) and MO (negative) have the similar molecular weight and different charges. MG has a positive charge and larger molecular weight than the other two dyes. Therefore, less flux of MG can be related to its higher molecular weight and adsorption on the membrane surface through electrostatic interactions.

3.1.4. Dye flux changes over time. Changes in dye flux over time are also surveyed for membranes M_1 and M_5, and the resulting plots are shown in Fig. 14. Despite the flux obtained for membrane M_5 is greater than membrane M_1, the flux drop (the plots slope) in membrane M_5 is higher than membrane M_1 and proves the effect of negative membrane surface charge and electrostatic interactions on dye adsorption. Therefore, in the M_5 membrane, the highest flux drop was observed in MG dye solution and MO has the lowest flux drop.
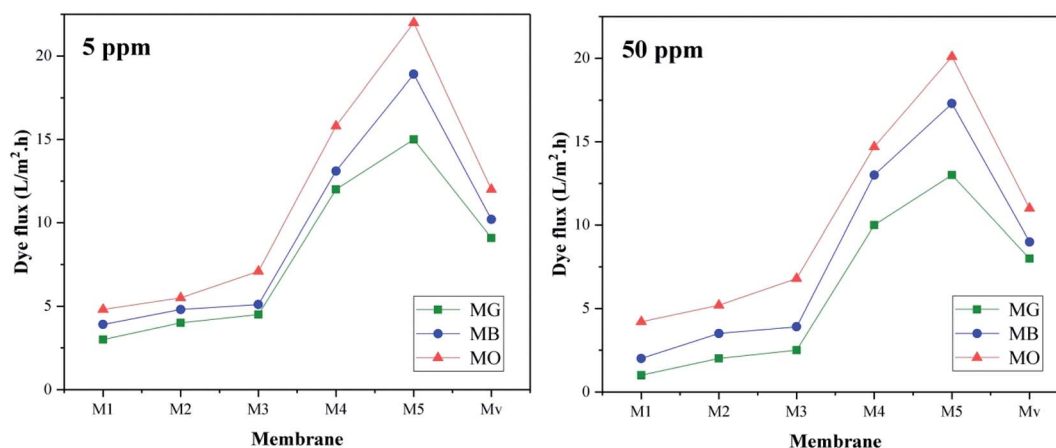

Fig. 13 Dye flux of membranes at different concentrations (5 and 50 ppm).
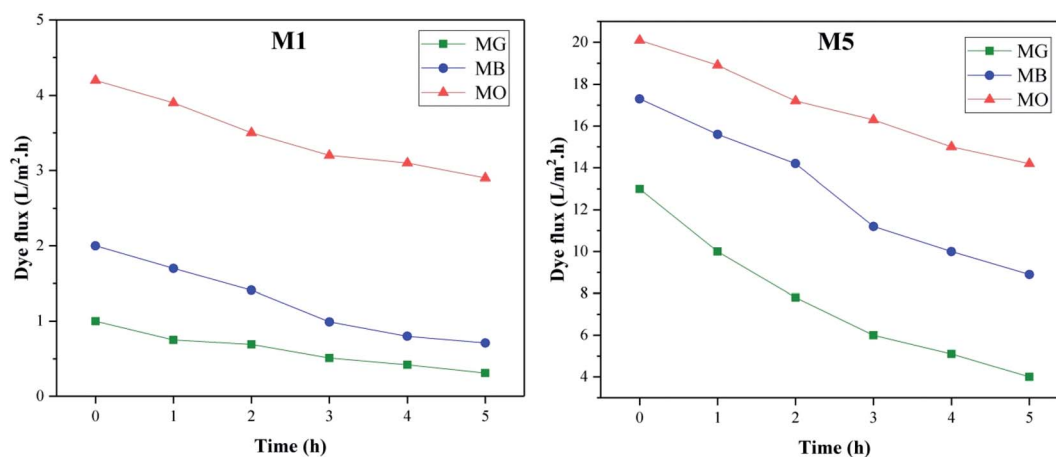

Fig. 14 Dye flux changes over time (0–5 h) for M_1 and M_5 membranes.
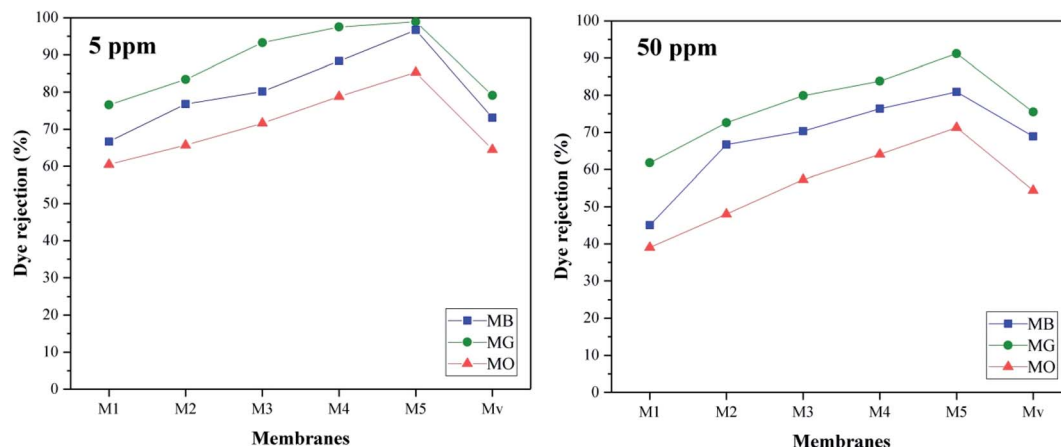
Fig. 15 Dye rejection of membranes at different concentrations.

Table 5 Dye rejection performance comparison with similar studies

Entry	Content	Dye rejection (%)	Pure water flux ($L\ m^{-2}\ h^{-1}$)	Ref.
1	$ABS/KCC-1-NH-CS_2$	MB: 98 MO: 82 MG: 99	37	Current study
2	Polyethersulfone/DADMAC-MWCNT	MB: 97.9 MO: 53.7	100	32
3	Polysulfone/MWCNT	Crystal violet (CV): 98.5	—	33
4	$Polysulfone/MIP-TiO_2$	Methylene blue: 95 Methylene orange: 34	14	34
5	PVDF/GO	Rhodamine B: 67.8%	62	35

3.1.5. Dye rejection. The performance of membranes in the removal of MG, MB, and MO dye solutions (5 and 50 ppm) is investigated and the results are shown in Fig. 15. Nanocomposite membranes have better performance than neat one in removing dyes and with increasing the percentage of additives, the membrane efficiency has improved. This progress is probably due to the effect of the interactions established between the functional groups in the membrane and the dyes, which has improved the ability of the membranes to remove dyes despite the enlargement of the pores.

The highest rejection efficiency is related to MG dye, which can be justified due to its larger size and electrostatic attraction interactions between the negative charge of the membrane surface and the positive charge of the dye. The decrease in the efficiency of membrane M_v compared to nanocomposite membranes containing $KCC-1-NH-CS_2$ is quite obvious. As the concentration of dye increases, the efficiency of the membranes in rejection process decreases. Due to the high concentration of dyes in the solution as well as the limited capacity of the membrane to absorb the dyes, this drop in yield seems normal.

The performance of our prepared nanocomposite membranes in dye rejection are compared with similar studies[32–35] and summarized in Table 5. Comparison of the data shows that membrane M_5, in addition to having a better efficiency in removing dyes, has better porosity and flux than pure membrane and due to its better hydrophilicity, shows less flux loss over time than membrane M_1.

4. Conclusion

In this study, ABS nanocomposite membranes with functionalized porous nanostructures ($KCC-1-NH-CS_2$) were fabricated by phase inversion. The utilization of this polymer due to its availability and low cost has provided a great advantage for making nanocomposite membranes and the introduction of $KCC-1-NH-CS_2$ nanostructures in addition to improving surface hydrophilicity, due to the presence of functional groups has played a significant role in improving membrane performance in removing dyes. The results showed that the water contact angle as a measure of surface hydrophilicity in membrane M_5 compared to membrane M_1 decreased from 79° to 67°. Water absorption (swelling degree) in membrane M_5 has increased by more than 100% compared to pure membrane, and this membrane, despite having high porosity (42%) and improved flux (35 $L\ m^{-2}\ h^{-1}$), has a better efficiency in removing dyes (MG: 99%, MB: 98%, MO: 82%).

Conflicts of interest

There are no conflicts to declare.

Acknowledgements

References

1 M. Pedro-Monzonís, A. Solera, J. Ferrer, T. Estrela and J. Paredes-Arquiola, *J. Hydrol.*, 2015, **527**, 482–493.

2 M. L. Sall, A. K. Diagne Diaw, D. Gningue-Sall, S. E. Aaron and J. J. Aaron, *Environ. Sci. Pollut. Res.*, 2020, **27**, 29927–29942.

3 M. Jaishankar, T. Tseten, N. Anbalagan, B. B. Mathew and K. N. Beeregowda, *Interdiscip. Toxicol.*, 2014, **7**, 60–72.

4 R. Li, L. Zhang and P. Wang, *Nanoscale*, 2015, **7**, 17167–17194.

5 K. C. Khulbe and T. Matsuura, *Nanotechnology in Membrane Processes*, ed. K. C. Khulbe and T. Matsuura, Springer International Publishing, Cham, 2021, pp. 199–343, DOI: 10.1007/978-3-030-64183-2_6.

6 M. Shannon, P. W. Bohn, M. Elimelech, J. G. Georgiadis, B. J. Mariñas and A. M. Mayes, *Nature*, 2008, **452**, 301–310.

7 T. Hillie and M. Hlophe, *Nat. Nanotechnol.*, 2007, **2**, 663–664.

8 M. Li, Z. Lv, J. Zheng, J. Hu, C. Jiang, M. Ueda, X. Zhang and L. Wang, *ACS Sustainable Chem. Eng.*, 2017, **5**, 784–792.

9 Z. Thong, G. Han, Y. Cui, J. Gao, T. S. Chung, S. Y. Chan and S. Wei, *Environ. Sci. Technol.*, 2014, **48**, 13880–13887.

10 M. Elimelech and W. A. Phillip, *Science*, 2011, **333**, 712–717.

11 N. AlSawaftah, W. Abuwatfa, N. Darwish and G. Husseini, *Water*, 2021, **13**, 1327.

12 H. Zhao, L. Feng, X. Ding, Y. Zhao, X. Tan and Y. Zhang, *J. Membr. Sci.*, 2018, **564**, 800–805.

13 S. Quan, S. W. Li, Y. C. Xiao and L. Shao, *Int. J. Greenhouse Gas Control*, 2017, **56**, 22–29.

14 G. Liu, Y. Labreche, V. Chernikova, O. Shekhah, C. Zhang, Y. Belmabkhout, M. Eddaoudi and W. J. Koros, *J. Membr. Sci.*, 2018, **565**, 186–193.

15 J. H. Lee, J. Hong, J. H. Kim, Y. S. Kang and S. W. Kang, *Chem. Commun.*, 2012, **48**, 5298–5300.

16 R. D. Solunke and G. Veser, *Fuel*, 2011, **90**, 608–617.

17 H. Wu, X. Li, Y. Li, S. Wang, R. Guo, Z. Jiang, C. Wu, Q. Xin and X. Lu, *J. Membr. Sci.*, 2014, **465**, 78–90.

18 S. E. Lehmana and S. C. Larsen, *Environ. Sci.: Nano*, 2014, **1**, 200–213.

19 M. W. Hakami, A. Alkhudhiri, S. Al-Batty, M.-P. Zacharof, J. Maddy and N. Hilal, *Membranes*, 2020, **10**, 248.

20 J. Yin and B. Deng, *J. Membr. Sci.*, 2015, **479**, 256–275.

21 S. Li, X. Jiang, H. Sun, S. He, L. Zhang and L. Shao, *J. Membr. Sci.*, 2019, **586**, 185–191.

22 S. Homaeigohar and M. Elbahri, *NPG Asia Mater.*, 2017, **9**, e427.

23 M. Dalwani, N. E. Benes, G. Bargeman, D. Stamatialis and M. Wessling, *J. Membr. Sci.*, 2011, **372**, 228–238.

24 F. S. Kamelian, E. Saljoughi, P. Shojaee Nasirabadi and S. M. Mousavi, *Polym. Compos.*, 2018, **39**, 2835–2846.

25 F. S. Kamelian, S. M. Mousavi and A. Ahmadpour, *Appl. Surf. Sci.*, 2015, **357**, 1481–1489.

26 M. Hapońska, E. Clavero, J. Salvadó, X. Farriol and C. Torras, *Algal Res.*, 2018, **33**, 118–124.

27 D. Ewis, N. A. Ismail, M. Hafiz, A. Benamor and A. H. Hawari, *Environ. Sci. Pollut. Res.*, 2021, **28**, 12256–12281.

28 A. R. Kamble, C. M. Patel and Z. V. P. Murthy, *Renewable Sustainable Energy Rev.*, 2021, **145**, 111062.

29 D. D. Kachhadiya and Z. V. P. Murthy, in *Handbook of Consumer Nanoproducts*, ed. S. Mallakpour and C. M. Hussain, Springer Singapore, Singapore, 2021, pp. 1–15, DOI: 10.1007/978-981-15-6453-6_86-1.

30 V. Polshettiwar, D. Cha, X. Zhang and J. M. Basset, *Angew. Chem., Int. Ed.*, 2010, **49**, 9652–9656.

31 M. Anvari Gharabaghlou and N. Shadjou, *Int. J. Environ. Sci. Technol.*, 2021, **18**, 1089–1096.

32 M. Mahmoudian, Y. Khazani, P. Gozali Balkanloo and M. Enayati, *Polym. Bull.*, 2021, **78**, 4313–4332.

33 F. Mustafanejad, N. Sajjadi, R. Marandi and M. Zaeimdar, *Nanotechnol. Environ. Eng.*, 2021, **6**, 1–9.

34 H. M. Ng, C. Leo and A. Abdullah, *J. Environ. Chem. Eng.*, 2017, **5**, 3991–3998.

35 Z. Zhu, L. Wang, Y. Xu, Q. Li, J. Jiang and X. Wang, *J. Colloid Interface Sci.*, 2017, **504**, 429–439.